

## High-strength Al-5Mg<sub>2</sub>Si-2Mg-2Fe alloy with extremely high Fe content for green industrial application through additive manufacturing

Jiaying Wang, Jianbao Gao, Hailin Yang, Feipeng Yang, Tao Wen, Zhilin Liu, Lijun Zhang & Shouxun Ji

To cite this article: Jiaying Wang, Jianbao Gao, Hailin Yang, Feipeng Yang, Tao Wen, Zhilin Liu, Lijun Zhang & Shouxun Ji (2023) High-strength Al-5Mg<sub>2</sub>Si-2Mg-2Fe alloy with extremely high Fe content for green industrial application through additive manufacturing, *Virtual and Physical Prototyping*, 18:1, e2235587, DOI: [10.1080/17452759.2023.2235587](https://doi.org/10.1080/17452759.2023.2235587)

To link to this article: <https://doi.org/10.1080/17452759.2023.2235587>



© 2023 The Author(s). Published by Informa UK Limited, trading as Taylor & Francis Group



[View supplementary material](#)



Published online: 20 Jul 2023.



[Submit your article to this journal](#)



Article views: 935



[View related articles](#)




[View Crossmark data](#)



Citing articles: 1 [View citing articles](#)

# High-strength Al–5Mg<sub>2</sub>Si–2Mg–2Fe alloy with extremely high Fe content for green industrial application through additive manufacturing

Jiaying Wang<sup>a</sup>, Jianbao Gao<sup>a</sup>, Hailin Yang <sup>a</sup>, Feipeng Yang<sup>a</sup>, Tao Wen<sup>a</sup>, Zhilin Liu<sup>b</sup>, Lijun Zhang<sup>a</sup> and Shouxun Ji<sup>c</sup>

<sup>a</sup>State Key Laboratory of Powder Metallurgy, Central South University, Changsha, People's Republic of China; <sup>b</sup>Light Alloy Research Institute, College of Mechanical and Electrical Engineering, Central South University, Changsha, People's Republic of China; <sup>c</sup>BCAST, Brunel University London, Uxbridge, UK

## ABSTRACT

Achieving superior mechanical properties of Al alloys with high content of Fe impurities is very challenging. Here, a feasible method was applied to accommodate high Fe content (~2.2 wt.%) and obtain superior strength in an Al–5Mg<sub>2</sub>Si–2Mg–2Fe alloy by using additive manufacturing. Heterogeneous distribution of Fe, including a high number density of  $\alpha$ -Al<sub>12</sub>(Fe,Mn)<sub>3</sub>Si particles distributed at the melting pool boundary and excessive Fe segregated along the cell boundaries that divided by Mg<sub>2</sub>Si eutectics, was verified as the beneficial factor for the alloy design and strength enhancement. In addition to the heterogeneous grains that contain fine cells, the interactions between dislocations and coherent Mg<sub>2</sub>Si eutectics and the  $\alpha$ -Al<sub>12</sub>(Fe, Mn)<sub>3</sub>Si particles played an important role in improving the mechanical properties. This work represents a breakthrough in recycling high-strength Al alloys with extremely high Fe doping for green industrial application through additive manufacturing.

## ARTICLE HISTORY

Received 23 April 2023  
Accepted 1 July 2023

## KEYWORDS



Additive manufacturing;  
Laser powder bed fusion;  
Aluminium alloys; Fe;  
Strengthening mechanisms


## 1. Introduction

Carbon-neutral has been globally set as an achievable goal for dealing with climate change in coming decades (Mallapaty 2020; Christensen and Bisinella 2021). The reduction of energy consumption in materials and structural manufacturing is an effective approach to achieving sustainable development for carbon-neutral. Among all available metallic materials, Al alloys have attracted much attention as candidate metals in structural applications, particularly when properties such as high specific strength are highly desired (Sun et al. 2019; Li et al. 2020). With the increasingly importance of circular economy and environmental concerns, the application of recycled Al alloys is becoming increasingly attractive. It is worth noting that compared with the production of primary Al alloys, recycling consumes only 5–10% of the total energy spent on primary ingot production in addition to reduce greenhouse gas emissions (Kevorkijian 2013; Gaustad, Olivetti, and Kirchain 2012; Nakajima et al. 2010). However, the recycled Al alloys are usually downgraded in mechanical properties (Zhang et al. 2012). The accumulation of impurities in

recycled Al alloys is a significant and long-term barrier, posing a bottleneck to their widespread use in industry. Therefore, the solutions to diminishing the detrimental effects of impurity elements or to tune these to beneficial effects are scientifically and technically vital.

On the different impurities in various Al alloys, Fe is always problematic because of its low equilibrium solubility in  $\alpha$ -Al solid solution (maximum ~0.052 wt.%) and the easy picking up during manufacturing (Ji et al. 2013). Most commercial wrought and cast Al alloys have Fe impurity around 0.2 wt.%, which increases further to a level of 0.3–0.8 wt.% or higher during recycling (Belov, Aksenov, and Eskin 2002), and its removal from Al melts is energy intensive and severely limited for thermodynamic reasons (Gaustad, Olivetti, and Kirchain 2012; Nakajima et al. 2010; Paraskevas et al. 2015). To diminish the detrimental effects of Fe, several different metallurgical solutions were used, i.e. (1) to avoid the formation of low symmetry Al–Fe or Al–Fe–Si compounds by lowering Fe levels as low as economically possible; (2) to modify the crystal structures from low symmetry compounds to high symmetry lattice types

**CONTACT** Hailin Yang  [lijun.zhang@csu.edu.cn](mailto:lijun.zhang@csu.edu.cn)  State Key Laboratory of Powder Metallurgy, Central South University, Changsha 410083, People's Republic of China

 Supplemental data for this article can be accessed online at <https://doi.org/10.1080/17452759.2023.2235587>

© 2023 The Author(s). Published by Informa UK Limited, trading as Taylor & Francis Group

This is an Open Access article distributed under the terms of the Creative Commons Attribution-NonCommercial License (<http://creativecommons.org/licenses/by-nc/4.0/>), which permits unrestricted non-commercial use, distribution, and reproduction in any medium, provided the original work is properly cited. The terms on which this article has been published allow the posting of the Accepted Manuscript in a repository by the author(s) or with their consent.

in castings (Narayanan, Samuel, and Gruzleski 1995) and (3) to refine the intermetallics by physical approaches including the use of superheated melt, solidification under high cooling rate (*CR*), and/or melt treatment (Fang et al. 2007). Unfortunately, it remains challenging to develop processes and/or methods suitable for industrial application of recycling Al alloys with high Fe contents (i.e. >1 wt.%).

Due to the rapid *CR* and complex thermodynamics of metal-based additive manufacturing (AM) process (Zhang et al. 2023; Zhang et al. 2019; Ding et al. 2022; Momeni et al. 2022), some unique advantages can be realised. First, the solid solubility limit can be improved significantly (Zhou et al. 2019; Sun et al. 2022); the unconventionally large amounts of slowly diffusing metal and/or rare earth elements, such as Sc and Zr, can now be placed into the solid solution, which is not possible in the traditional metallurgy processes (Li et al. 2020; Kuo et al. 2020). Second, AM process has a potential to change the sequence of phase formation (Sun et al. 2021; Zhu et al. 2022). It was found that the dendritic regions in the Al<sub>0.5</sub>CoCrFeNi alloy only consists of the primary face-centred cubic (fcc) phase because the B2/body-centred cubic (bcc) phase is kinetically suppressed by the fast *CR* (Sun et al. 2021); the uncommon metastable (Mg,Zn,Cu)-rich icosahedral quasicrystal (*I*-phase) aligned as a filigree skeleton could be detected in the additively manufactured AlZnMgCuScZr alloy (Zhu et al. 2022). Third, the excessive Al/Si (Sun et al. 2021), Cr (Voisin et al. 2021), Mn (Wei et al. 2022) and even for refractory metal elements Mo (Gao et al. 2020) and Zr (Li et al. 2020) have been found to segregate at cell boundaries. The cell boundary segregation engineering has been proved to deliver grain refinement and inhibit the formation of hot tearing and brittle intermetallic compounds (Li et al. 2020; Sun et al. 2021; Voisin et al. 2021; Gao et al. 2020). However, whether AM can apply these advantages to Al alloys with high Fe content is still unknown.

It has been recently shown that the addition of extra 2 wt.% Mg reduced the solidification range and improved the eutectic level in the Al–5Mg<sub>2</sub>Si alloy fabricated by laser powder bed fusion (LPBF), which delivered superior yield strength (295.0 MPa) and elongation (9.3%) (Yang et al. 2021). The novel alloy with low cost and good formability has great potential applications in industry. Based on our long-term studies on Al alloys and their recycling (Yang, Ji, and Fan 2015; Zhu et al. 2021), in this work we try to employ LPBF further to control solidification and accommodate the extremely high Fe content (~2.2%) and investigate Fe distribution in the Al–5Mg<sub>2</sub>Si–2Mg alloy. The high Fe doping is experimentally proved to be beneficial for the alloy design and

strength enhancement, demonstrating that additive manufacturing is an effective strategy to mitigate the detrimental effects of unwanted impurities in recycled Al alloys for industrial applications.

## 2. Experimental section

### 2.1. Powder and materials fabrication

Pre-alloyed Al–5Mg<sub>2</sub>Si–2Mg–2Fe alloy powder was produced by gas atomisation. High purity argon was used as the protective atmosphere to avoid oxidation during atomisation. Chemical composition of the pre-alloyed powder was analysed by inductively coupled plasma atomic emission spectrometry (ICAP 7000 Series) and given in Table 1. The powder particles were of spherical morphology with a few of smaller satellite particles (Figure 1a). Few flaws were observed in the cross-section of the powder particles, and fine eutectic Mg<sub>2</sub>Si phase 2–5 μm in size was distributed between α-Al dendrites (Figure 1b and c).

The LPBF process was conducted using an FS271 (Farsoon, Inc., China) machine equipped with an ytterbium fibre laser (IPG YLR-500-WC, Germany). The parameters were adopted as follows: laser beam diameter, laser powder (*P*), scan speed (*v*), hatch spacing (*h*) and layer thickness (*t*) are 90 μm, 270 W, 1000 mm/s, 0.10 and 0.05 mm, respectively. The samples were built layer-by-layer on a plate of 6061 Al alloy, which was grit-blasted with alumina prior to installation. The laser scanning strategy was set to be 67° rotating scanning layer-by-layer, as shown in Figure 1(d). Ageing was carried out in an electric resistance furnace that was preheated to a given temperature and maintained the temperature consistently for at least 1 h before putting the as-LPBFed samples into the chamber of the furnace. The ageing temperature and time were 180°C and 3.5 h respectively. The samples were taken out from the furnace for air cooling after ageing.

### 2.2. Microstructural characterisations

Phase constituents were identified by X-ray diffraction (XRD) using a Rigaku X-2000 diffractometer with Cu *K*<sub>α</sub> radiation ( $\lambda_{K\alpha} = 1.54 \text{ \AA}$ ) at 40 kV. The spectra were recorded in the angular range of 30–80° (2θ) with the

**Table 1.** The composition of experimental Al–5Mg<sub>2</sub>Si–2Mg–2Fe powder calibrated by ICP-AES.

Allloys	Mg	Si	Mn	Fe	Others	Al
Al–5Mg <sub>2</sub> Si–2Mg–2Fe (wt.%)	5.40	2.64	0.80	2.22	<0.08	Bal.

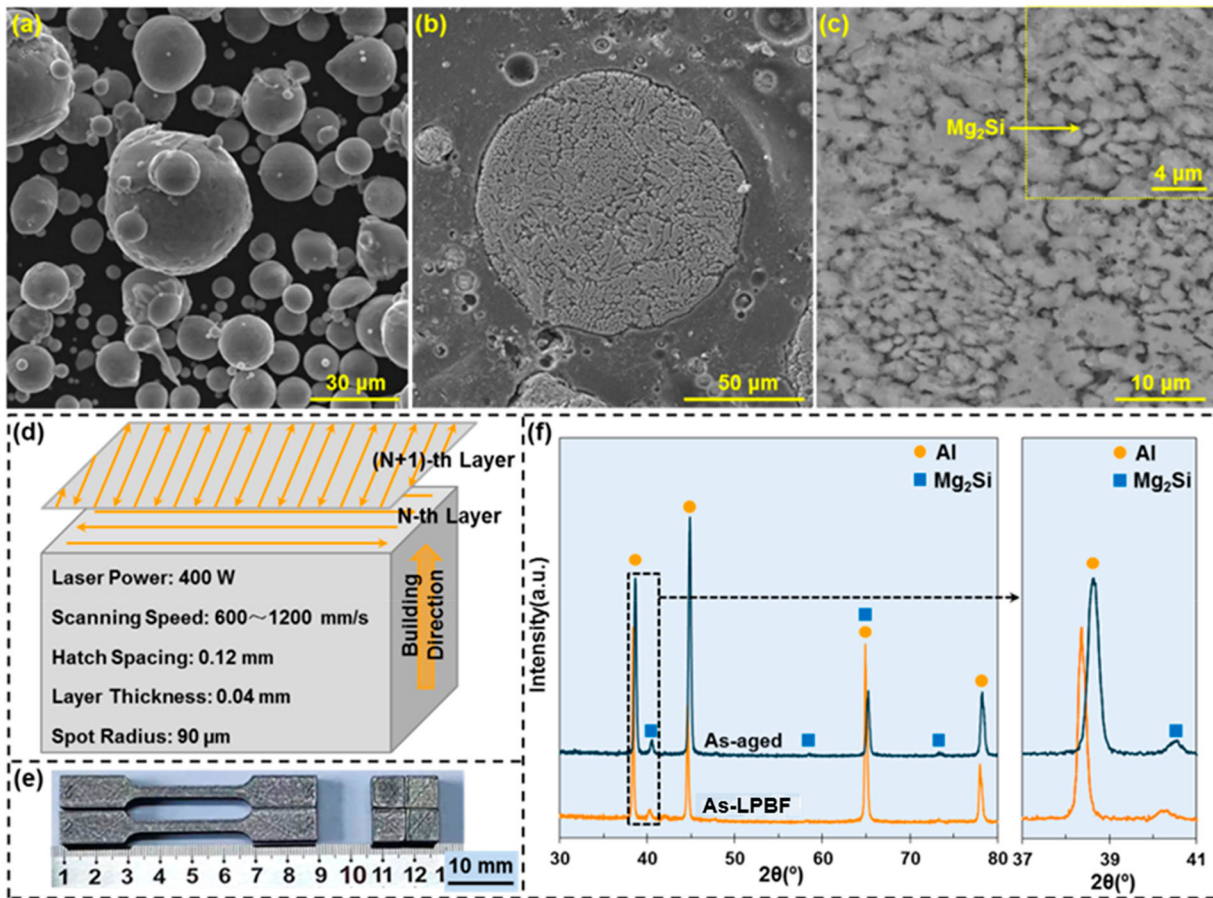


**Figure 1.** SEM image showing (a) the surface morphologies and (b,c) the cross-sectioned morphologies of pre-alloyed Al-5Mg<sub>2</sub>Si-2Mg-2Fe powder; (d) schematic diagram of laser beam scanning procedure; (e) optical micrograph showing the tensile samples and square samples; (f) XRD spectra of the Al-5Mg<sub>2</sub>Si-2Mg-2Fe alloy under as-LPBFed and as-aged conditions.

scanning step of 0.05°. The dislocation density was estimated by means of the Williamson–Hall method (Cauwenbergh et al. 2021) based on the XRD pattern. Microstructure features of the alloy were analysed using multiple electron microscopes. Scanning electron microscope (SEM) and electron backscattered diffraction (EBSD) orientation mappings were conducted in an FIB Helios NanoLab G3 UC system equipped with a Hikari camera and the TSL OIM data analysis software for EBSD. Before SEM and EBSD, the samples were polished using 40 nm colloidal silica suspension. Detailed microstructure was further characterised using transmission electron microscope (TEM: Tecnai G2 F20) operating at 200 kV. TEM samples were prepared by combination of mechanical polishing and precision ion polishing system (PIPS) at a voltage/an incident angle of 2–5 kV/3–8°. The average diameter and volume fraction of the fine cell (typical structure of LPBF) and *in-situ* particles are measured by Image-Pro Plus with high angle annular dark field (HAADF) TEM images. All the microstructural characteristics were detected along the horizontal direction of samples.

### 2.3 . Mechanical tests

Dog-bone-shaped tensile samples were with a gauge length of 30 mm and cross-section of 4 mm × 2 mm, as indicated in Figure 1(e). Both sides of the specimens were carefully ground to a 2000 grit finish using an SiC paper. Uniaxial tensile tests were performed using a material testing system (MTS Alliance RT30) at room temperature with an engineering strain rate of  $1 \times 10^{-3} \text{ s}^{-1}$ . Square-shaped samples (10 mm × 10 mm × 2 mm) were used for micro-hardness test by Vickers hardness (ASTM E384-08) under a load of 100 g for 15 s. Each reported data was the average of at least three to five measurements.

## 3. Results and discussion

### 3.1. Microstructure

LPBF method with high solidification velocity ( $SV$ ) and large thermal gradient ( $G$ ) usually promotes the formation of unusual microstructure (Zhang et al. 2019; Zhou et al. 2019; Sun et al. 2022). The hierarchical



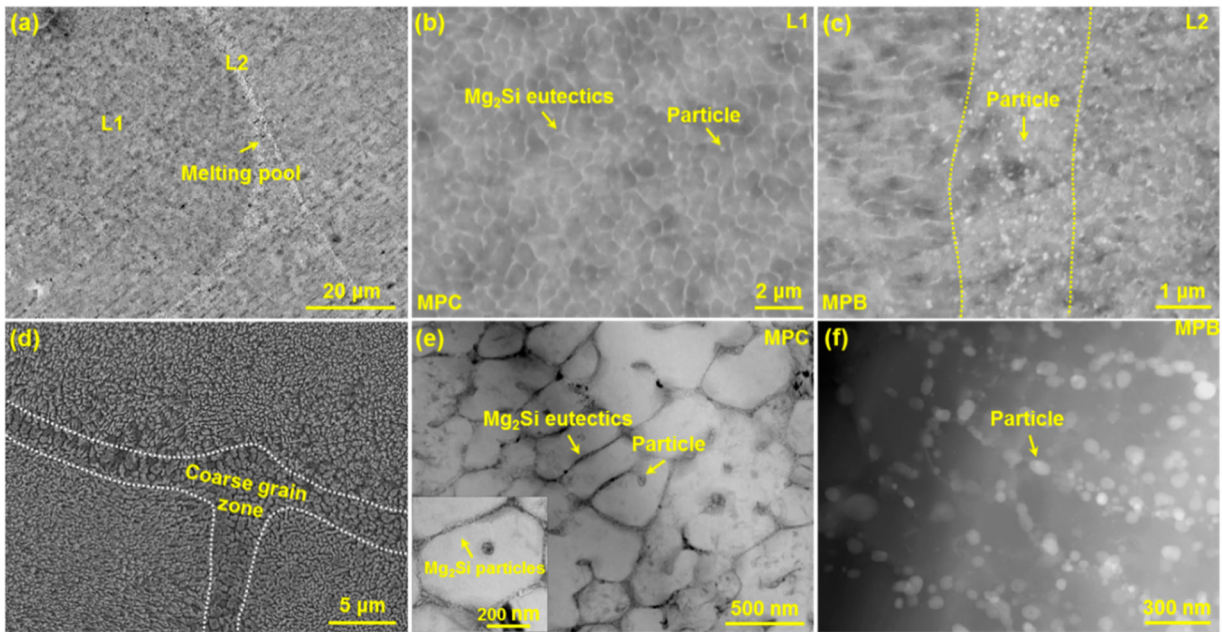


**Figure 2.** (a–d) SEM and (e,f) TEM images showing the microstructure of as-LPBFed Al–5Mg<sub>2</sub>Si–2Mg–2Fe alloy; (a) the overall microstructure; (b,c) the detailed microstructure in zone L1 and zone L2, respectively; (d) the overall microstructure after deep etching; (e) BF-TEM image showing the detailed microstructure in zone L1; (f) STEM image displaying the detailed microstructure in zone L2.

microstructure of the Al–5Mg<sub>2</sub>Si–2Mg–2Fe alloy is dominated by the melting pools (Figure 2a). The equiaxed cells ( $\sim 0.58 \mu\text{m}$ ) with boundaries of Mg<sub>2</sub>Si eutectics and a small number of nano-sized white particles are detected in the zone of melting pool centre (MPC, Figure 2b), while a large amount of white particles are observed in the zone of melting pool boundary (MPB, Figure 2c). The equiaxed cells existed across the whole sections (see deep etching image in Figure 2d), with the only difference being the relatively coarse grains in the MPB zone. TEM images in Figure 2(e–f) show that the eutectics are composed of Mg<sub>2</sub>Si particles and the numerous white particles (10–100 nm in size) are distributed in the MPC zone and MPB zone, respectively.

Details of microstructure and the interface between  $\alpha$ -Al matrix and Mg<sub>2</sub>Si/particles are shown in Figure 3(a–d). High-resolution (HR) TEM image (Figure 3c) and inserted selected area electron diffraction (SAED) pattern (L1) imply that there is an orientation relationship (OR) at the interface of Al/Mg<sub>2</sub>Si:  $[011](020)//[\bar{1}12](1\bar{1}1)$ . The Mg<sub>2</sub>Si phase is coherent with  $\alpha$ -Al matrix along  $[\bar{1}12]$  direction, with an interplanar spacing of 0.206 nm for  $(020)_{\text{Al}}$  plane of  $\alpha$ -Al matrix and 0.394 nm for  $(1\bar{1}1)_{\text{Mg}_2\text{Si}}$  plane of Mg<sub>2</sub>Si phase. Previous study has shown that the formation of Al–Mg<sub>2</sub>Si eutectics in as-LPBFed Al alloys helps to mitigate hot cracking by eutectic feeding during solidification (Li et al. 2020).

It is worth noting that the interface of Al/particle have a coherent OR with  $[110](111)//[110](111)$  (Figure 3d). The particle is coherent with  $\alpha$ -Al matrix along  $[110]$

direction, with an interplanar spacing of 0.925 nm for  $(111)$  plane of the particle. The interface of Al/particle also have a coherent OR with  $[001](020)//[001](020)$  (Figure S1). A coherent OR between Al matrix and Mg<sub>2</sub>Si as well as particles builds a solid basis for the ductility of alloy (Yang et al. 2021). Meanwhile, HR-TEM images in Figure 3(c<sub>2</sub>, d<sub>2</sub>) indicate the interactions between dislocations and Mg<sub>2</sub>Si as well as particles. The elastic energy introduced by the lattice misfit at the interface provides the required driving force for the formation of interfacial dislocations, thus providing a solid basis for the strength of alloy (Røyset and Ryum 2015).

LPBF method with high SV and large G also promotes element segregation (Li et al. 2020; Sun et al. 2021; Voisin et al. 2021; Wei et al. 2022). The elemental mapping of the MPC zone and MPB zone is shown in Figure 3(e, e<sub>1</sub>–e<sub>5</sub>) and Figure 3(f, f<sub>1</sub>–f<sub>5</sub>), respectively. Mg and Si are distributed along the cell boundaries, confirming that Al–Mg<sub>2</sub>Si eutectics are formed in a divorced approach and no traditional lamellae structure is present in the eutectic cells. Figure 3(f, f<sub>1</sub>–f<sub>5</sub>) confirm that the *in-situ* particles distributed at the MPB zone are enriched in Al, Fe, Mn and Si elements. It is also noted that a low number density of particles distributed within or at the cell boundaries are  $\alpha$ -Al<sub>12</sub>(Fe,Mn)<sub>3</sub>Si, clarified by the elemental mapping and EDS point analysis in Figure 3(b) (see Table 2). Similar microstructure has been reported in Al–6Mg–2.3Si–0.8Mn–0.3Fe (wt.%) alloy (Warmuzek et al. 2021). Remaining Mn is presented

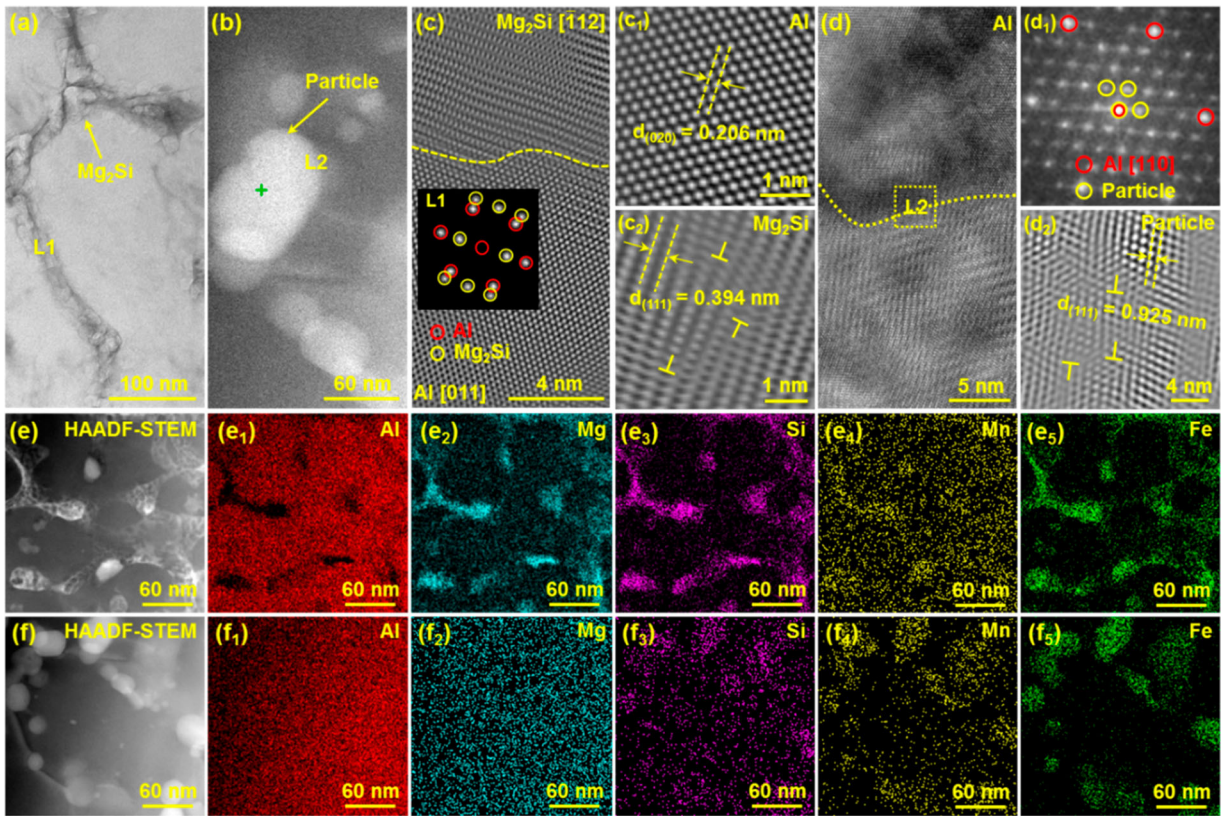


**Figure 3.** Details of TEM analysis of microstructure of the as-LPBFed Al-5Mg<sub>2</sub>Si-2Mg-2Fe alloy: (a–d) the interface relationships between Al matrix and Mg<sub>2</sub>Si as well as white particles; (e, e<sub>1</sub>–e<sub>5</sub>; f, f<sub>1</sub>–f<sub>5</sub>) showing the elemental mapping of the cells and MPB zone where particle enriches, respectively.

within  $\alpha$ -Al matrix, while Fe segregates at the cell boundaries. The average compositions of different regions measured by quantitative TEM/EDX analysis are shown in Figure S2 and Table 2. The solid solubility of Fe at high CR significantly increased to 0.22–0.25%, compared to the low value of  $\sim$ 0.052 wt.% in cast/wrought Al alloys (Ji et al. 2013); Fe content at the cell boundaries is up to  $\sim$ 13.52 wt.%. Additionally, EDX showed that Fe concentration in the MPB zone is  $\sim$ 2.04 wt.%, higher than  $\sim$ 1.83 wt.% in the MPC zone.

SEM and TEM micrographs of as-aged Al-5Mg<sub>2</sub>Si-2Mg-2Fe alloy are shown in Figures 4 and 5. Similarly to the as-LPBFed alloy, the typical microstructure is controlled by melting pools. The equiaxed cells with boundaries of Mg<sub>2</sub>Si eutectics and a small number of  $\alpha$ -Al<sub>12</sub>(Fe,

Mn)<sub>3</sub>Si particles are detected in MPC zone (Figure 4b), while a large amount of  $\alpha$ -Al<sub>12</sub>(Fe,Mn)<sub>3</sub>Si particles are observed in MPB zone (Figure 4c). Moreover, BF-TEM and STEM images (Figure 4d,e) show the existence of boundary between MPC where eutectic Mg<sub>2</sub>Si phase enriches and MPC where  $\alpha$ -Al<sub>12</sub>(Fe,Mn)<sub>3</sub>Si particle enriches. Particularly, nano-sized *in-situ* Mg<sub>2</sub>Si particles (about 5–15 nm in size) are detected in the eutectic cell zones (Figure 4f), indicating that a subsequent direct aging exhibits strong precipitation strengthening effects. In the XRD spectra in Figure 1(f), the peaks of Mg<sub>2</sub>Si in the as-LPBFed samples are weaker than those in the as-aged samples, indicating that more Mg<sub>2</sub>Si phases were formed during ageing, which is also the potential reason that the peak of (111)Al in the as-LPBFed alloy shifts to a higher  $2\theta$  angle. Within the cells, the  $\alpha$ -Al<sub>12</sub>(Fe,Mn)<sub>3</sub>Si particles are of a relatively low density, as shown by the STEM image in Figure 4(g).

BF-TEM and HR-TEM images of the *in-situ* Mg<sub>2</sub>Si particles within cell boundaries are shown in Figure 5(a and b). The Mg<sub>2</sub>Si eutectic phase along [011] direction, with an interplanar spacing of 0.385 nm for (11 $\bar{1}$ )<sub>Mg2Si</sub> planes of the Mg<sub>2</sub>Si eutectic phase, and 0.374 nm for (11 $\bar{1}$ )<sub>Mg2Si</sub> planes of *in-situ* Mg<sub>2</sub>Si particles, as shown in the fast Fourier transform (FFT) patterns (L1&L2).

**Table 2.** Average compositions (wt.%) of the different regions measured by quantitative TEM/EDX analysis (Figure 4b and Figure S2) in the as-LPBFed Al-5Mg<sub>2</sub>Si-2Mg-2Fe alloy.

Alloy	Mg	Si	Mn	Fe	Al
Point of L2 (Figure 4b) wt.%	0.01	5.12	6.33	7.85	80.69
Zone of L1 (Figure S2a) wt.%	3.78	0.24	0.41	0.25	95.32
Zone of L2 (Figure S2a) wt.%	13.82	8.11	2.42	13.52	62.13
EDX mapping (Figure S2a) wt.%	6.01	1.63	0.70	1.83	89.83
Zone of L3(Figure S2b) wt.%	3.40	0.29	0.43	0.22	95.66
EDX mapping (Figure S2b) wt.%	5.65	1.50	0.73	2.04	90.08



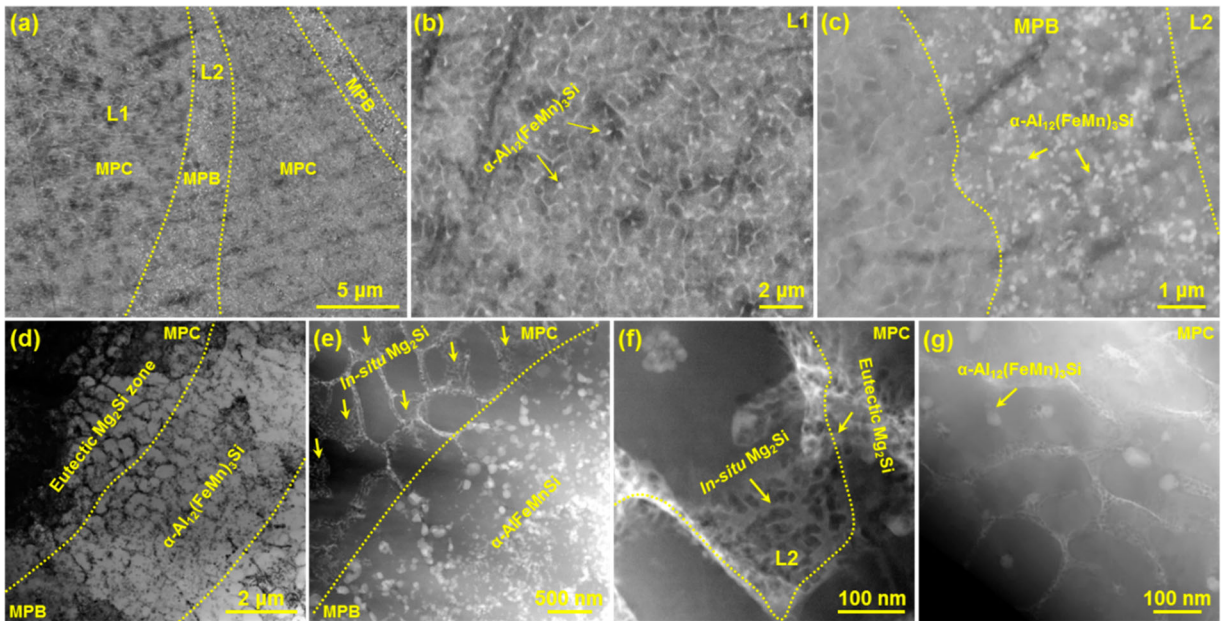


**Figure 4.** SEM/TEM images showing the as-LPBFed Al-5Mg<sub>2</sub>Si-2Mg-2Fe alloy with ageing at 180°C for 3.5 h; (a,d,e) the overall microstructure; the detailed microstructure in zone L1 (b) and zone L2 (c); (f) the formation of *in-situ* Mg<sub>2</sub>Si particles with eutectic network; (g) the formation of low number density of  $\alpha$ -Al<sub>12</sub>(Fe,Mn)<sub>3</sub>Si particle at the MPC zone.

Meanwhile, a large amount of  $\alpha$ -Al<sub>12</sub>(Fe,Mn)<sub>3</sub>Si particles are observed in MPB zone (Figure 5c). HAADP-STEM images and the elemental mapping of various areas are shown in Figure 5(d–f). In the eutectic area, Mg, Si and Fe are enriched in the cell boundaries, and Al, Fe, Mn and Si are enriched in *in-situ*  $\alpha$ -Al<sub>12</sub>(Fe,Mn)<sub>3</sub>Si particles, as shown in Figure 5(d, d<sub>1</sub>–d<sub>5</sub>). A large amount of *in-situ* particles within cell boundaries are enriched in Mg and Si (Figure 5(e, e<sub>1</sub>–e<sub>5</sub>)), confirming the formation of Mg<sub>2</sub>Si particles. The eutectic Mg<sub>2</sub>Si phases were also observed in the MPB zone where  $\alpha$ -Al<sub>12</sub>(Fe,Mn)<sub>3</sub>Si particles enriched, indicating that the eutectic cells existed in the whole sections (Figure 5(f, f<sub>1</sub>–f<sub>5</sub>)).

LPBF with high CR normally delivers fine grain size. The microstructure shows obvious fine heterogeneous equiaxed grains at a size of 5–15  $\mu$ m coupled with ultrafine grains at a size of 0.5–1.0  $\mu$ m in the local areas (Figure 6a), due to remelting (Thijs et al. 2013). The columnar grains with sizes of 15–80  $\mu$ m in length and 3–15  $\mu$ m in width are detected along the building direction (Figure 6b); some regions in the conjunction areas of the columnar grains also contain fine equiaxed grains. Inoculation is generally practiced as an important technique to promote microstructural refinement (Liu et al. 2014). Comparing the Al-5Mg<sub>2</sub>Si-2Mg alloy (Figure S3; Wang et al. 2022), the high Fe doping reduces grain size significantly: 7.8  $\mu$ m (horizontal direction) and 15.8  $\mu$ m (building direction) in the Al-5Mg<sub>2</sub>Si-2Mg-2Fe alloy, in counterpart with 13.2  $\mu$ m (horizontal

direction) and 19.0  $\mu$ m (building direction) in the Al-5Mg<sub>2</sub>Si-2Mg alloy.

### 3.2. Phase diagrams

The microstructural characteristics indicate that the as-LPBFed Al-5Mg<sub>2</sub>Si-2Mg-2Fe alloy exhibits superior processability. Based on the Cost 507 thermodynamic database, equilibrium phase diagram and vertical cross-section along the Al-xMg<sub>2</sub>Si, Al-xMg<sub>2</sub>Si-2Mg and Al-5Mg<sub>2</sub>Si-2Mg-xFe alloys were calculated. It is seen that 2 wt.% Mg addition leads to a decrease the liquidus temperature and phase range between  $\alpha$ -Al and (L +  $\alpha$ -Al + Mg<sub>2</sub>Si) for Al-xMg<sub>2</sub>Si alloys (Figure 7a). Fe doping promotes the formation of  $\alpha$ -Al(FeMn)Si phase, and the primary phase change from  $\alpha$ -Al phase to  $\alpha$ -Al(FeMn)Si phase in the Al-5Mg<sub>2</sub>Si-2Mg alloy when Fe content is higher than 0.878 wt.% (Figure 7b).

It is worth noting that Fe doping also has a potential to decrease hot tearing susceptibility. The crack susceptibility index (CSI) of the Al-5Mg<sub>2</sub>Si-2Mg alloy tends to decrease from 4371.3°C to 11.8°C with 2 wt.% Fe addition (Figure 7c). The solidification sequence of Al-5Mg<sub>2</sub>Si-2Mg-2.2Fe-0.8Mn alloy is: L  $\rightarrow$   $\alpha$ -Al(FeMn)Si, L  $\rightarrow$  ( $\alpha$ -Al +  $\alpha$ -Al(FeMn)Si), L  $\rightarrow$  ( $\alpha$ -Al +  $\alpha$ -Al(FeMn)Si + Mg<sub>2</sub>Si), as predicted by the Scheil-Gulliver model in Figure 7(d) (Gulliver 1913).  $\alpha$ -Al(FeMn)Si and Mg<sub>2</sub>Si phases form when the temperature is below 693.44°C and 592.68°C, respectively. The equilibrium phase fractions of  $\alpha$ -Al(FeMn)Si and Mg<sub>2</sub>Si phases reach to the



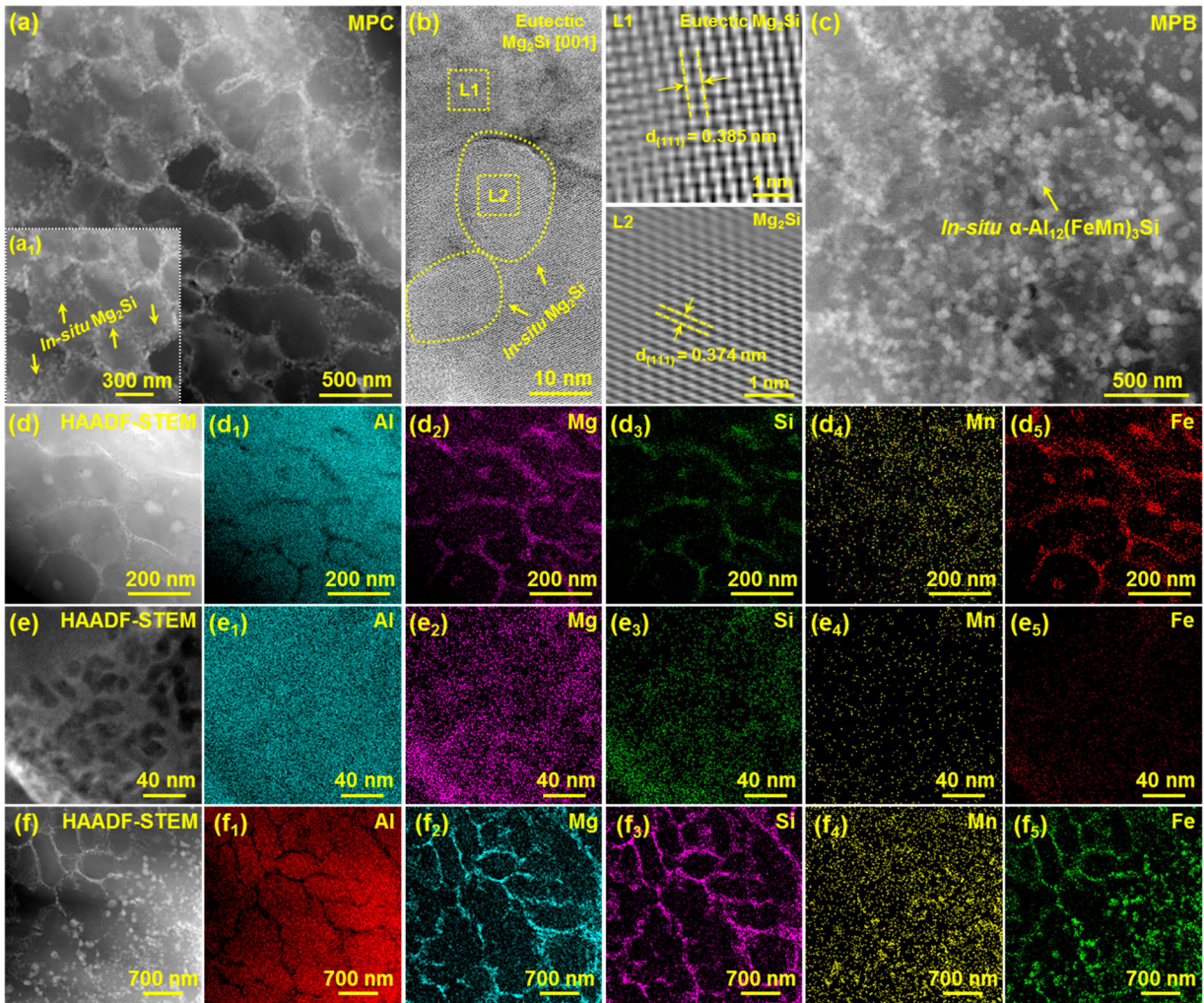


**Figure 5.** Detailed TEM analysis of as-LPBFed Al-5Mg<sub>2</sub>Si-2Mg-2Fe alloy with ageing at 180°C for 3.5 h; (a,b,L1,L2) the formation of Mg<sub>2</sub>Si particles within Mg<sub>2</sub>Si eutectics; (c) the formation of high number density  $\alpha$ -Al<sub>12</sub>(Fe,Mn)<sub>3</sub>Si particle at the MPB zone; (d, d<sub>1</sub>-d<sub>5</sub>) EDS maps of Mg<sub>2</sub>Si eutectics; (e, e<sub>1</sub>-e<sub>5</sub>) EDS maps of *in-situ* Mg<sub>2</sub>Si particles; (f, f<sub>1</sub>-f<sub>5</sub>) EDS maps of  $\alpha$ -Al<sub>12</sub>(Fe,Mn)<sub>3</sub>Si particles distributed at MPB zone.

maximum values (5.6% and 6.8%) when the temperature is below 400°C. Based on the calculation results, the high Fe doping is not the hindrance of alloy design.

Based on the microstructural characteristics, four characteristics of Fe heterogeneous distribution in the Al-5Mg<sub>2</sub>Si-2Mg-2Fe alloy are: (1) a high solid solubility

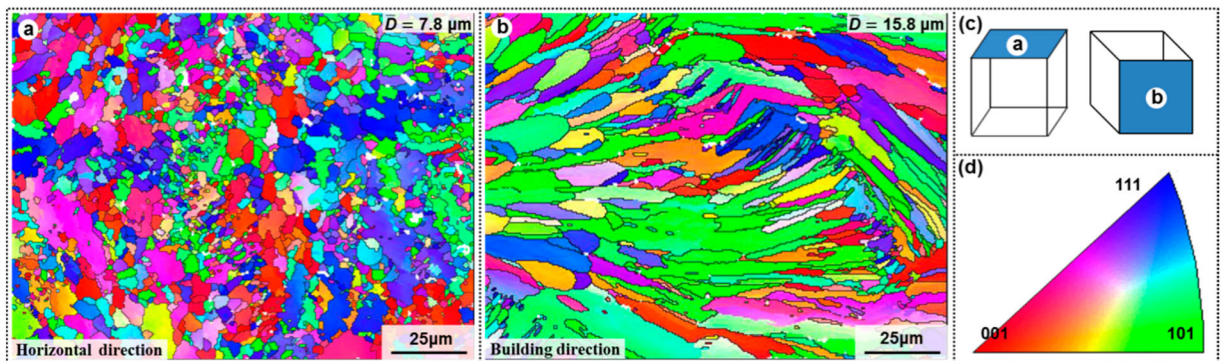


**Figure 6.** EBSD-inverse pole figures (IPFs) of the as-LPBFed Al-5Mg<sub>2</sub>Si-2Mg-2Fe alloy along (a) horizontal and (b) building directions; (c) schematic images showing the direction of samples; (d) corresponding IPF map.



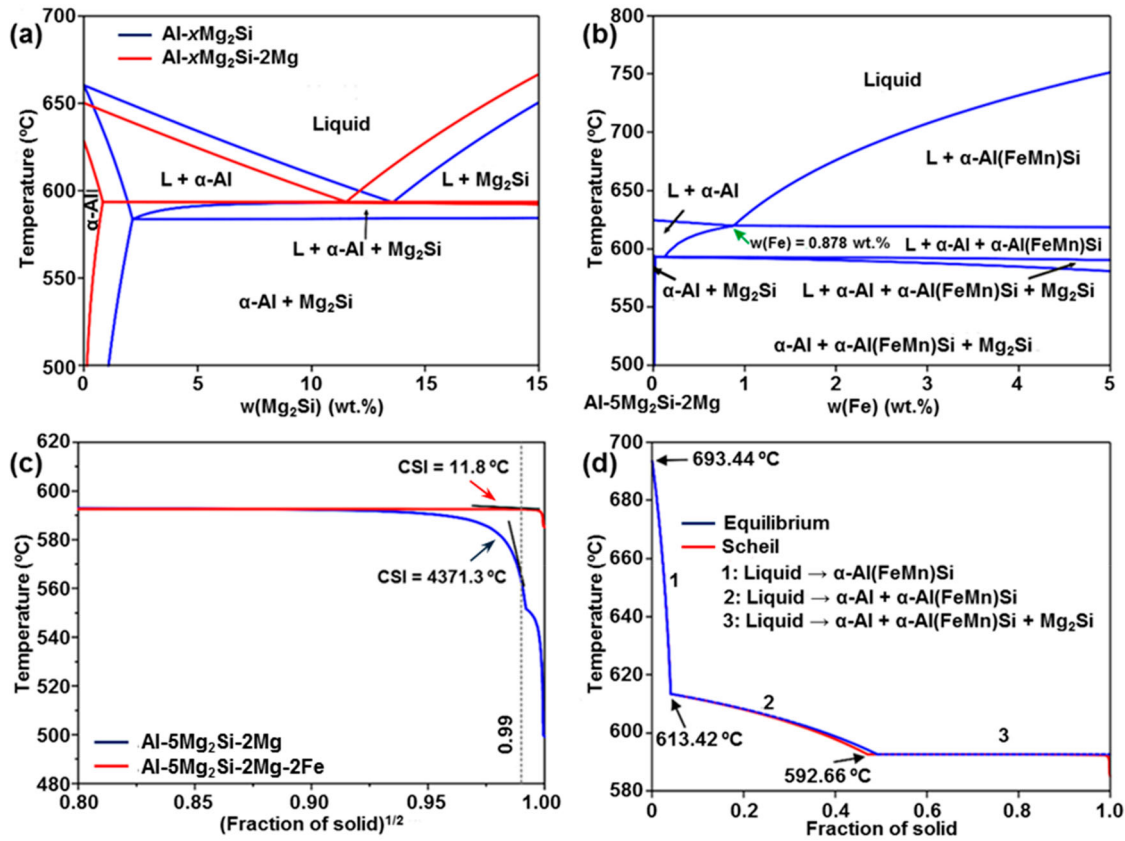


**Figure 7.** (a) Equilibrium phase diagram of Al–Mg<sub>2</sub>Si and Al–5Mg<sub>2</sub>Si–2Mg alloy; (b) vertical cross-section of Al–5Mg<sub>2</sub>Si–2Mg–xFe alloy; (c) the crack susceptibility index (CSI) calculated via  $T$  vs.  $(f_s)^{1/2}$  curves of Al–5Mg<sub>2</sub>Si–2Mg–xFe alloy; (d) Scheil solidification simulation of the Al–5Mg<sub>2</sub>Si–2Mg–2.2Fe–0.8Mn alloy.

of Fe; (2) a large amount of Fe segregated at the cell boundaries that divided by Mg<sub>2</sub>Si eutectics; (3) the formation of a large number of α-Al<sub>12</sub>(Fe,Mn)<sub>3</sub>Si particles in the MPB zone and (4) a relatively higher Fe content detected in the MPB zone, in counterpart with that of in the MPC zone. The difference in composition

between the boundary and interior of cells suggests a significant partitioning among elements between the liquid and solid phases during LPBF process (Wei et al. 2022; Gao et al. 2020); a strong particle accumulation effect induced by high temperature gradient is also a possible reason for the element segregation at the cell

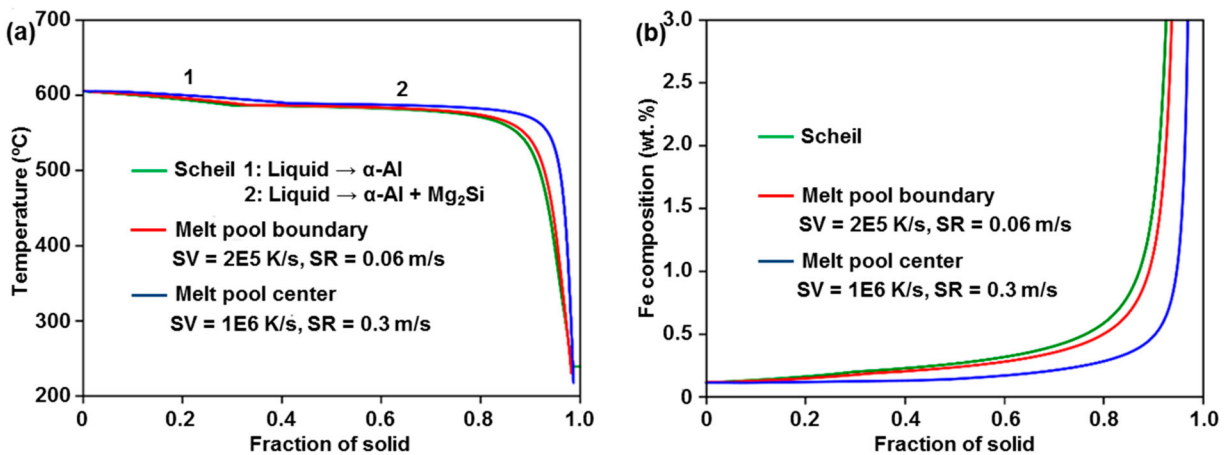


**Figure 8.** The effects of high SV on (a) the solidification path (b) the Fe solubility in α-Al considering the α-Al phase as the primary phase.

**Table 3.** Kinetic parameters for the Al–5Mg<sub>2</sub>Si–2Mg–2Fe alloy.

Parameter	Value	Unit	Description	Ref
$\gamma$	0.163	J/m <sup>2</sup>	Solid/liquid interfacial energy	Zhang et al. 2020
$\Delta H_f$	$1.36 \times 10^9$	J/m <sup>3</sup>	Heat of fusion	Zhang et al. 2020
$g$	30	NA	Geometric factor for coarsening	Zhang et al. 2020
$v_0$	1000	m/s	Kinetic pre-factor for $\Delta T_k$	Zhang et al. 2020
$a_0$	1	Nm	Solute trapping parameter	Zhang et al. 2020
$G$	...	K/m	Thermal gradient	
$SV$	...	m/s	Solidification velocity	
$CR$	...	K/s	Cooling rate: $CR = G \times SV$	

boundary (Ji et al. 2020). It is worth mentioning that the second layer of the samples provides a heat treatment for the first layer during LPBF process that involves a layer-by-layer printing, which temporarily raises the temperature of MPB zone so that Fe atoms at these positions are re-precipitated to increase the volume fraction of  $\alpha$ -Al<sub>12</sub>(Fe,Mn)<sub>3</sub>Si particles.

Supersaturated solid solutions are formed inevitably in the printed microstructures during the rapid cooling ( $10^5$ – $10^6$  K/s) (Cauwenbergh et al. 2021). In this work, supersaturated solid solutions tend to form in  $\alpha$ -Al phase because the high  $CR$  hardly affects the solubility of Fe in the primary  $\alpha$ -Al<sub>12</sub>(Fe,Mn)<sub>3</sub>Si phase (see Figure 7b). In general, the solidification condition depends on the depth of melting pool (Sonawane et al. 2021). The  $G$  of MPC zone is lower than that of the MPB zone, while the  $SV$  of MPC is higher than that of the MPB zone. Figure 8 shows the effects of  $SV$  on the solidification path and solid solubility of Fe in  $\alpha$ -Al matrix (considering the  $\alpha$ -Al phase as the primary phase), and the kinetic parameters are listed in Table 3. It is worth noting that a high  $SV$  causes the solute trapping, resulting in the partition coefficient ( $k_v$ ) far from the partitioning parameter ( $k_e$ ). With increasing  $SV$ , the solidification path is far away from the Scheil solidification (Figure 8a), and the solid solubility of Fe in the MPC zone is slightly lower than that in the MPB zone with the same solid

fraction (Figure 8b). This is in agreement with the experimental results (Table 2).

### 3.3. Mechanical properties

Based on the above results, high Fe doping brings advantages, including (1) an obvious decrease in the CSI of Al–5Mg<sub>2</sub>Si–2Mg alloy, which is beneficial to the alloy design for LPBF; (2) a significant decrease in the grain size of  $\alpha$ -Al matrix; (3) the formation of  $\alpha$ -Al<sub>12</sub>(Fe, Mn)<sub>3</sub>Si particles with a high number density and (4) Fe segregation at the cell boundaries. The unique hierarchical microstructure induced by these characteristics builds a solid foundation for strength enhancement. Comparing with the as-LPBFed Al–5Mg<sub>2</sub>Si–2Mg alloy without high Fe doping (Yang et al. 2021), the as-LPBFed Al–5Mg<sub>2</sub>Si–2Mg–2Fe alloy shows substantially increased strengths, including the ultimate tensile strength (UTS) of 498.3 MPa, yield strength (YS) of 346.9 MPa and elongation of 10.3% (Figure 9a). The following ageing also introduced significant improvement in the strength, with UTS, YS and elongation being 545.3, 390.5 MPa and 8.4%, respectively. A few of pores with the relatively shallow dimples are observed in the fracture surfaces of the as-LPBFed alloy (Figure 9b and c), consistent with the good ductility. Meanwhile, as shown in Figure 9(d), the Al–5Mg<sub>2</sub>Si–2Mg–2Fe alloy

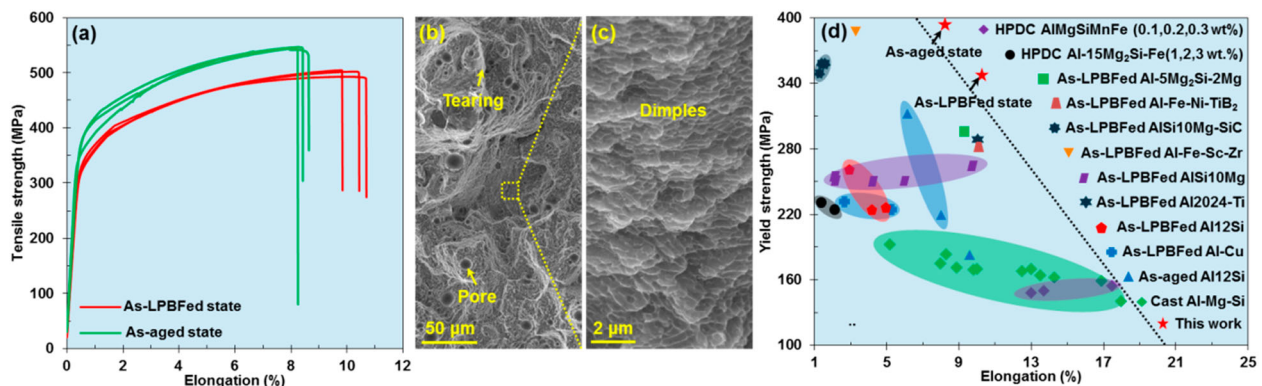


**Figure 9.** (a) Tensile stress-strain curves of the Al–5Mg<sub>2</sub>Si–2Mg–2Fe alloy without and with ageing treatment; (b,c) tensile fractured morphology; (d) comparison of the tensile properties between the Al–5Mg<sub>2</sub>Si–2Mg–2Fe alloy in this study and other Al alloys fabricated by casting, LPBF and HPDC methods.



exhibits a giant response for a superior comprehensive mechanical response when compared the other Al alloys fabricated by various methods, including casting, LPBF and HPDC methods (Yang et al. 2021; Wang et al. 2018; Tan et al. 2020; Wei et al. 2017; Aboulkhair et al. 2016; Fousová et al. 2018; Patakham et al. 2021; Li et al. 2015; Prashanth et al. 2014; Wang et al. 2014; Zhu et al. 2019; Park et al. 2021; Ji et al. 2012; Emamy et al. 2013; Wang et al. 2021; Tan et al. 2020; Feng et al. 2022; Ji et al. 2023).

To understand the mechanisms underlying the improved strength of the Al-5Mg<sub>2</sub>Si-2Mg-2Fe alloy without and with ageing, the deformation substructures were characterised via TEM (Figure 10). As expected, a large number density of dislocations interacted with Mg<sub>2</sub>Si eutectics can be detected at the MPC zone (Figure 10a), and the interaction between dislocations and *in-situ* Mg<sub>2</sub>Si particles can be also observed at the MPC zone of the as-aged alloy (Figure 10c). Meanwhile, the interaction between spherical heterogeneous

$\alpha$ -Al<sub>12</sub>(Fe,Mn)<sub>3</sub>Si particles distributed at the MPB zone and dislocations leads to an effective Zener pinning effect (Moelans, Blanpain, and Wollants 2007) (Figure 10b,d); gliding dislocations also have a potential to cut through the coherent ultrafine  $\alpha$ -Al<sub>12</sub>(Fe,Mn)<sub>3</sub>Si among heterogeneous particles, which build a basis for ductility enhancement (Ming, Bi, and Wang 2018).

From the above microstructural observations, the newly developed alloy with unique hierarchical microstructure delivers superior mechanical properties. The increase in strength arises from the multiple potential strengthening mechanisms, including solid solution strengthening ( $\sigma_s$ ), grain refinement ( $\sigma_g$ ), precipitating strengthening ( $\sigma_p$ ) and dislocation strengthening ( $\sigma_{dis}$ ), in addition to its lattice friction strength ( $\sigma_0$ ). The overall YS ( $\sigma_y$ ) is expressed as follows:

$$\sigma_y = \sigma_0 + \sigma_g + \sigma_{dis} + \sigma_p + \sigma_s \quad (1)$$

where  $\sigma_0$  is the matrix strength ( $\sim 10$  MPa) that is the maximum shear stress necessary for dislocation glide

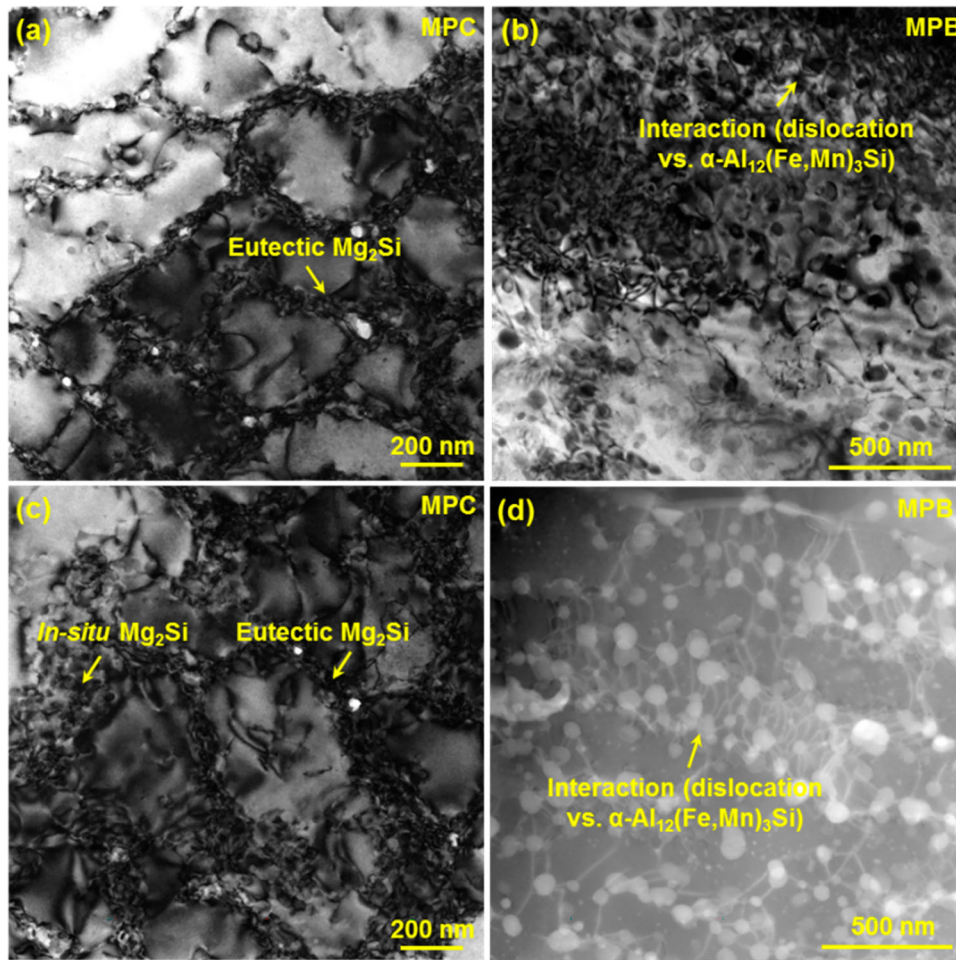


**Figure 10.** TEM analysis of the (a,b) as-LPBFed and (c,d) as-aged Al-5Mg<sub>2</sub>Si-2Mg-2Fe alloy after tensile testing: (a) the interaction between dislocations and Mg<sub>2</sub>Si eutectics at the MPC zone; (c) the interaction between dislocations and Mg<sub>2</sub>Si eutectics and *in-situ* Mg<sub>2</sub>Si particles at the MPC zone; (b,d) The interaction between dislocations and  $\alpha$ -Al<sub>12</sub>(Fe,Mn)<sub>3</sub>Si particles at the MPB zone.

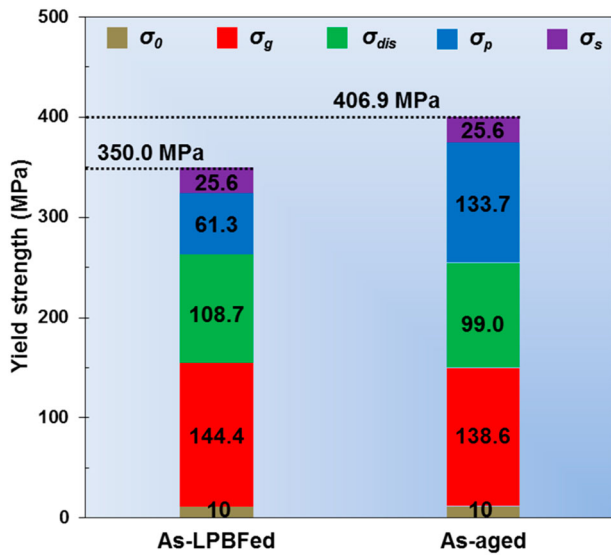


**Figure 11.** The contributions of different strengthening mechanisms to the YS.

in pure Al (Jia et al. 2019). Correspondingly, the contributions from all these strengthening effects are displayed in Figure 11 (as presented in Supplementary Note 2; Meanwhile, Figure S4 and Figure S5 were introduced to calculate the strength contribution of

dislocation strengthening and precipitation strengthening to yield strength, respectively.), of which the summations (350.0 and 406.9 MPa) are slightly higher than that of the experimentally measured YS values (346.9 and 390.5 MPa).

Another feature for the designed alloy is that a promising uniform elongation is still achieved. The relative high ductility might be originated from the effective strain hardening rate induced from heterogeneous Al matrix (0.5–15  $\mu\text{m}$ ). Although relatively coarse grains among the refined heterogeneous grains sacrifice strengthening effect gained from fine grains, coarse grains have a good strain hardening effect due to the accumulation of dislocations and stabilisation of tensile deformation, resulting in a good ductility (Wang et al. 2020). It is worth noting that the increase in both YS and UTS without apparently sacrificing ductility is partially ascribed to ultrafine coherent  $\text{Mg}_2\text{Si}$  eutectics and  $\alpha\text{-Al}_{12}(\text{Fe,Mn})_3\text{Si}$  particles, the ultralow elastic interfacial strain from the coherent interface can avoid the accumulation of dislocations near the interface. Hence, the stress concentration around the particles can be relieved and the uniform plastic deformation can be maintained (Jiang et al. 2017). Previous study indicated that the heterogeneous nano-sized precipitates with

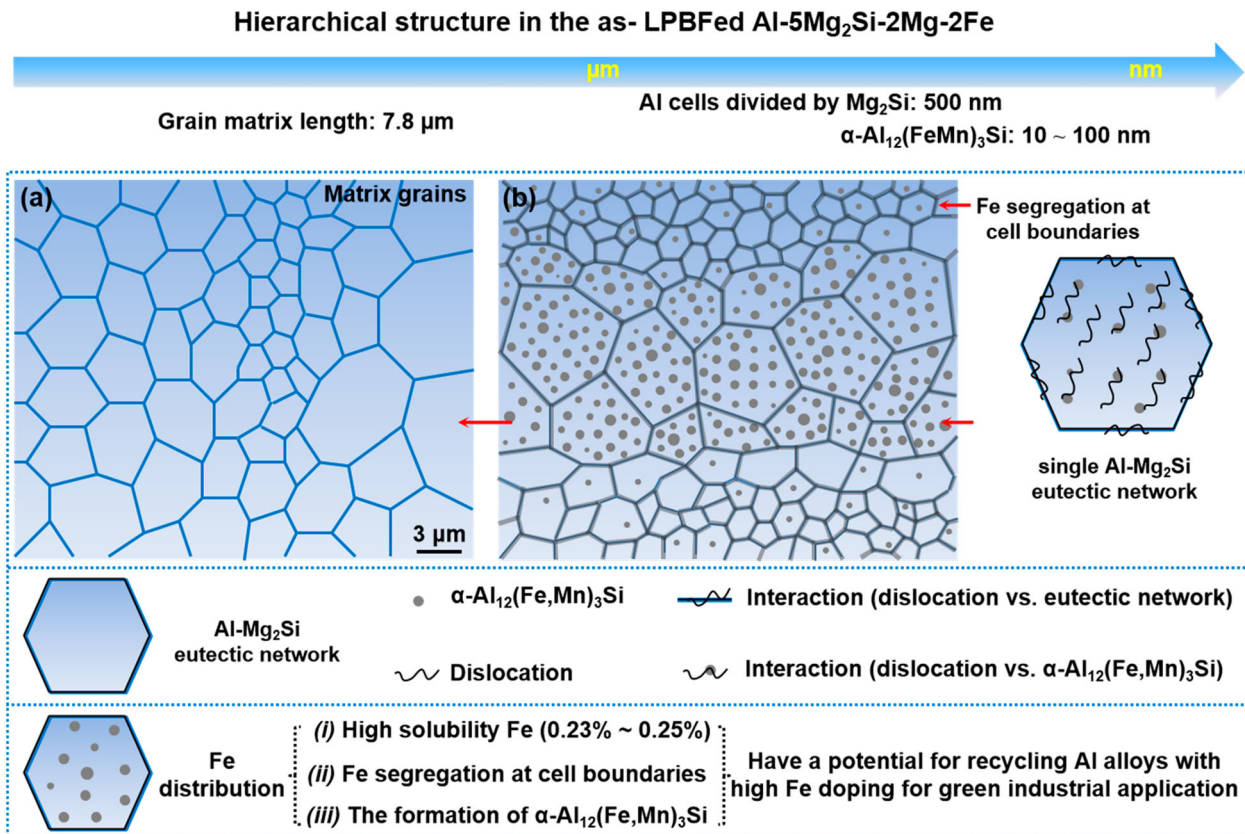


**Figure 12.** Schematic image showing the microstructural characteristics in this work.



different sizes brought the non-uniform strain distributions and promoted strain partitioning (Du et al. 2020), the heterogeneous  $\alpha$ -Al<sub>12</sub>(Fe,Mn)<sub>3</sub>Si particles (10–100 nm) also have a potential to reduce the loss of ductility via avoiding dislocation pile-ups and the stress concentration.

Overall, a representative diagram showing microstructural characteristics of the unique hierarchical structure in the studied Al–5Mg<sub>2</sub>Si–2Mg–2Fe alloy is schematically illustrated in Figure 12. The refined heterogeneous matrix grains (0.5–15  $\mu$ m) that contains ultrafine Al–Mg<sub>2</sub>Si eutectics and interactions between a high number density dislocations and coherent  $\alpha$ -Al<sub>12</sub>(Fe,Mn)<sub>3</sub>Si particles brought superior mechanical properties. Based on the above results, three positive findings are summarised: (i) the Al–5Mg<sub>2</sub>Si–2Mg–2Fe alloy with superior mechanical properties reveals that additive manufacturing can be an effective strategy to mitigate detrimental effects of unwanted elements in Al alloys; (ii) the work consider as a breakthrough in recycled Al alloys with high Fe doping for green industrial application; (iii) the composition of high-strength Al–5Mg<sub>2</sub>Si–2Mg–2Fe alloy also exhibits the advantage of cost control in counterpart with other as-LPBFed Al alloy with Sc/Zr doping.

#### 4. Summary and conclusion

In this work, LPBF method was applied to control the solidification process and accommodate extremely high Fe content (~2.2%) in a novel Al–5Mg<sub>2</sub>Si–2Mg alloy. The alloy samples before and after ageing offers excellent mechanical properties. The main conclusions can be drawn as follows:

1. Phase diagram calculation indicated that high Fe doping promotes the formation of  $\alpha$ -Al<sub>12</sub>(Fe,Mn)<sub>3</sub>Si phase and has the potential to decrease the crack susceptibility index and hot tearing susceptibility of the Al–5Mg<sub>2</sub>Si–2Mg alloy. The high Fe doping is not the hindrance of alloy design.
2. The novel characteristics of Fe heterogeneous distribution in the Al–5Mg<sub>2</sub>Si–2Mg–2Fe alloy were achieved: (1) a high solid solubility of Fe in Al matrix; (2) a large amount of Fe segregated at the cell boundaries that divided by Mg<sub>2</sub>Si eutectics; (3) the formation of a large number of  $\alpha$ -Al<sub>12</sub>(Fe,Mn)<sub>3</sub>Si particles in the MPB zone; and (4) a relatively higher Fe content in the MPB zone, in comparison with that in the MPC zone.
3. Comparing with Al–5Mg<sub>2</sub>Si–2Mg alloy with Fe in impurity level, the Al–5Mg<sub>2</sub>Si–2Mg–2Fe alloy shows substantially increased strengths: with the UTS, YS

and elongation being 498.3 MPa and 545.3 MPa, 346.9 and 390.5 MPa, and 10.3% and 8.4% at as-LPBFed and as-aged states, respectively. In addition to the heterogeneous grains that contained fine cells, the interaction between dislocations and Mg<sub>2</sub>Si eutectics as well as  $\alpha$ -Al<sub>12</sub>(Fe,Mn)<sub>3</sub>Si particles played an important role in improving the mechanical properties.

4. This work represents a breakthrough in development of high-strength Al alloys with extremely high Fe doping through additive manufacturing, demonstrating that additive manufacturing is an effective strategy to mitigate detrimental effects of unwanted elements in recycled Al alloys for industrial applications.

#### Acknowledgements

Hailin Yang acknowledges the financial support from the National Key Research and Development Program of China (grant number 2020YFB0311300ZL), National Natural Science Foundation of China (grant number 52071343) and Leading Innovation and Entrepreneurship Team of Zhejiang Province – Automotive Light Alloy Innovation Team (2022R01018) are gratefully acknowledged. Lijun Zhang acknowledges the financial support from the Science and Technology Program of Guangxi province, China (grant number AB21220028) and the Natural Science Foundation of Hunan Province for Distinguished Young Scholars (grant number 2021JJ10062).

#### Data availability statement

The data that support the findings of this study are available from the corresponding author upon reasonable request.

#### Disclosure statement

No potential conflict of interest was reported by the author(s).

#### Funding

This work was supported by National Key Research and Development Program of China: [Grant Number 2020YFB0311300ZL]; National Natural Science Foundation of China: [Grant Number 52071343]; Science and Technology Program of Guangxi province, China: [Grant Number AB21220028]; Natural Science Foundation of Hunan Province for Distinguished Young Scholars: [Grant Number 2021JJ10062].

#### ORCID

Hailin Yang  <http://orcid.org/0000-0003-3924-200X>

#### References

Aboulkhair, N. T., I. Maskery, C. Tuck, I. Ashcroft, and N. M. Everitt. 2016. "The Microstructure and Mechanical

- Properties of Selectively Laser Melted AlSi10Mg: The Effect of a Conventional T6-Like Heat Treatment." *Materials Science and Engineering: A* 667: 139–146. <https://doi.org/10.1016/j.msea.2016.04.092>.
- Belov, N. A., A. A. Aksenov, and D. G. Eskin. 2002. *Iron in Aluminium Alloys: Impurity and Alloying Elements*. New York, NY, USA: Taylor & Francis.
- Cauwenbergh, P. V., V. Samaee, L. Thijs, J. Nejezchlebová, and K. Vanmeensel. 2021. "Plasma Hsp90 Levels in Patients with Systemic Sclerosis and Relation to Lung and Skin Involvement: A Cross-Sectional and Longitudinal Study." *Scientific Reports* 11: 1–15. <https://doi.org/10.1038/s41598-020-79139-8>.
- Christensen, T., and V. Bisinella. 2021. "Climate Change Impacts of Introducing Carbon Capture and Utilisation (CCU) in Waste Incineration." *Waste Management* 126: 754–770. <https://doi.org/10.1016/j.wasman.2021.03.046>.
- Ding, H., C. Y. Zeng, J. Rausch, K. Momeni, and S. Guo. 2022. "Developing Fused Deposition Modeling Additive Manufacturing Processing Strategies for Aluminum Alloy 7075: Sample Preparation and Metallographic Characterization." *Materials* 15: 1340. <https://doi.org/10.3390/ma15041340>.
- Du, X. H., W. P. Li, H. T. Chang, T. Yang, G. S. Duan, B. L. Wu, J. C. Huang, et al. 2020. "Dual Heterogeneous Structures Lead to Ultrahigh Strength and Uniform Ductility in a Co–Cr–Ni Medium-Entropy Alloy." *Nature Communications* 11: 2390. <https://doi.org/10.1038/s41467-020-16085-z>.
- Emamy, M., A. R. Emami, R. Khorshidi, and M. R. Ghorbani. 2013. "The Effect of Fe-Rich Intermetallics on the Microstructure, Hardness and Tensile Properties of Al–Mg<sub>2</sub>Si die-Cast Composite." *Materials & Design (1980-2015)* 46: 881–888. <https://doi.org/10.1016/j.matdes.2012.11.041>.
- Fang, X., G. Shao, Y. Q. Liu, and Z. Fan. 2007. "Effects of Intensive Forced Melt Convection on the Mechanical Properties of Fe Containing Al–Si Based Alloys." *Materials Science and Engineering: A* 445–446: 65–72. <https://doi.org/10.1016/j.msea.2006.09.038>.
- Feng, Z., H. Tan, Y. B. Fang, X. Lin, and W. D. Huang. 2022. "Selective Laser Melting of TiB<sub>2</sub>/AlSi10Mg Composite: Processability, Microstructure and Fracture Behavior." *Journal of Materials Processing Technology* 299: 117386–117400. <https://doi.org/10.1016/j.jmatprotec.2021.117386>.
- Fousová, M., D. Dvorský, A. Michalcová, and D. Vojtěch. 2018. "Changes in the Microstructure and Mechanical Properties of Additively Manufactured AlSi10Mg Alloy After Exposure to Elevated Temperatures." *Materials Characterization* 137: 119–126. <https://doi.org/10.1016/j.matchar.2018.01.028>.
- Gao, S. B., Z. H. Hu, M. Duchamp, P. S. Sankara Rama Krishnan, S. Tekumalla, X. Song, and M. Seita. 2020. "Recrystallization-based Grain Boundary Engineering of 316L Stainless Steel Produced via Selective Laser Melting." *Acta Materialia* 200: 366–377. <https://doi.org/10.1016/j.actamat.2020.09.015>.
- Gaustad, G., E. Olivetti, and R. Kirchain. 2012. "Improving Aluminum Recycling: A Survey of Sorting and Impurity Removal Technologies." *Resources, Conservation and Recycling* 58: 79–87. <https://doi.org/10.1016/j.resconrec.2011.10.010>.
- Gulliver, G. M. 1913. "The Quantitative Effect of Rapid Cooling upon the Constitution of Binary Alloys." *The Journal of the Institute of Metals* 9: 120–157.
- Ji, Y. C., C. F. Dong, D. C. Kong, and X. G. Li. 2020. "Design Materials Based on Simulation Results of Silicon Induced Segregation at AlSi10Mg Interface Fabricated by Selective Laser Melting." *Journal of Materials Science & Technology* 46: 145–155. <https://doi.org/10.1016/j.jmst.2020.01.037>.
- Ji, X. H., S. F. Li, X. Zhang, L. Liu, S. L. Li, L. Gao, X. Li, and S. D. Wang. 2023. "Influence of Characteristic Parameters of SiC Reinforcements on Mechanical Properties of AlSi10Mg Matrix Composites by Powder Metallurgy." *Journal of Materials Research and Technology* 24: 6843–6853. <https://doi.org/10.1016/j.jmrt.2023.04.262>.
- Ji, S., D. Watson, Z. Fan, and M. White. 2012. "Development of a Super Ductile Diecast Al–Mg–Si Alloy." *Materials Science and Engineering: A* 556: 824–833. <https://doi.org/10.1016/j.msea.2012.07.074>.
- Ji, S. X., W. C. Yang, F. Gao, D. Watson, and Z. Y. Fan. 2013. "Effect of Iron on the Microstructure and Mechanical Property of Al–Mg–Si–Mn and Al–Mg–Si Diecast Alloys." *Materials Science and Engineering: A* 564: 130–139. <https://doi.org/10.1016/j.msea.2012.11.095>.
- Jia, Q., P. Rometsch, P. Kürnsteiner, Q. Chao, A. Huang, M. Weyland, L. Bourgeois, and X. Wu. 2019. "Selective Laser Melting of a High Strength Al Mn Sc Alloy: Alloy Design and Strengthening Mechanisms." *Acta Materialia* 171: 108–118. <https://doi.org/10.1016/j.actamat.2019.04.014>.
- Jiang, S. H., H. Wang, Y. Wu, X. J. Liu, H. H. Chen, M. J. Yao, B. Gault, et al. 2017. "Ultrastrong Steel via Minimal Lattice Misfit and High-Density Nanoprecipitation." *Nature* 544: 460–464. <https://doi.org/10.1038/nature22032>.
- Kevoorkian, V. 2013. "Challenges and Advantages of Recycling Wrought Aluminium Alloys from Lower Grades of Metallurgically Clean Scrap." *Materials Technology* 47: 13–23.
- Kuo, C. N., C. K. Chua, P. C. Peng, Y. W. Chen, S. L. Sing, S. Huang, and Y. L. Su. 2020. "Microstructure Evolution and Mechanical Property Response via 3D Printing Parameter Development of Al–Sc Alloy." *Virtual and Physical Prototyping* 15: 120–129. <https://doi.org/10.1080/17452759.2019.1698967>.
- Li, R. D., M. B. Wang, Z. M. Li, P. Cao, T. C. Yuan, and H. B. Zhu. 2020. "Developing a High-Strength Al–Mg–Si–Sc–Zr Alloy for Selective Laser." *Acta Materialia* 193: 83–98. <https://doi.org/10.1016/j.actamat.2020.03.060>.
- Li, X. P., X. J. Wang, M. Saunders, A. Suvorova, L. C. Zhang, Y. J. Liu, M. H. Fang, Z. H. Huang, and T. B. Sercombe. 2015. "A Selective Laser Melting and Solution Heat Treatment Refined Al–12Si Alloy with a Controllable Ultrafine Eutectic Microstructure and 25% Tensile Ductility." *Acta Materialia* 95: 74–82. <https://doi.org/10.1016/j.actamat.2015.05.017>.
- Liu, Z. L., D. Qiu, F. Wang, J. A. Taylor, and M. X. Zhang. 2014. "The Grain Refining Mechanism of Cast Zinc Through Silver Inoculation." *Acta Materialia* 79: 315–326. <https://doi.org/10.1016/j.actamat.2014.07.026>.
- Mallapaty, S. 2020. "How China Could be Carbon Neutral by mid-Century." *Nature* 586: 482–483. <https://doi.org/10.1038/d41586-020-02927-9>.
- Ming, K. S., X. F. Bi, and J. Wang. 2018. "Realizing Strength-Ductility Combination of Coarse-Grained Al<sub>0.2</sub>Co<sub>1.5</sub>CrFeNi<sub>1.5</sub>Ti<sub>0.3</sub> Alloy via Nano-Sized, Coherent Precipitates." *International Journal of Plasticity* 100: 177–191. <https://doi.org/10.1016/j.ijplas.2017.10.005>.
- Moelans, N., B. Blanpain, and P. Wollants. 2007. "Pinning Effect of Second-Phase Particles on Grain Growth in Polycrystalline Films Studied by 3-D Phase Field Simulations." *Acta Materialia* 55: 2173–2182. <https://doi.org/10.1016/j.actamat.2006.11.018>.



- Momeni, K., S. Neshani, C. Uba, H. Ding, J. Raush, and S. Guo. 2022. "Engineering the Surface Melt for in-Space Manufacturing of Aluminum Parts." *Journal of Materials Engineering and Performance* 31: 6092. <https://doi.org/10.1007/s11665-022-07054-2>.
- Nakajima, K., O. Takeda, T. Miki, K. Matsubae, S. Nakamura, and T. Nagasaka. 2010. "Thermodynamic Analysis of Contamination by Alloying Elements in Aluminum Recycling." *Environmental Science & Technology* 44: 5594–5600. <https://doi.org/10.1021/es9038769>.
- Narayanan, L. A., F. H. Samuel, and J. E. Gruzleski. 1995. "Dissolution of Iron Intermetallics in Al-Si Alloys Through Nonequilibrium Heat Treatment." *Metallurgical and Materials Transactions A* 26: 2161–2174. <https://doi.org/10.1007/BF02670687>.
- Paraskevas, D., K. Kellens, W. Dewulf, and J. R. Duflou. 2015. "Environmental Modelling of Aluminium Recycling: A Life Cycle Assessment Tool for Sustainable Metal Management." *Journal of Cleaner Production* 105: 357–370. <https://doi.org/10.1016/j.jclepro.2014.09.102>.
- Park, T. H., M. S. Baek, H. Hyer, Y. Sohn, and K. A. Lee. 2021. "Effect of Direct Aging on the Microstructure and Tensile Properties of AlSi10Mg Alloy Manufactured by Selective Laser Melting Process." *Materials Characterization* 176: 111113. <https://doi.org/10.1016/j.matchar.2021.111113>.
- Patakham, U., A. Palasay, P. Wila, and R. Tong Sri. 2021. "MPB Characteristics and Si Morphologies on Mechanical Properties and Fracture Behavior of SLM AlSi10Mg." *Materials Science and Engineering: A* 821: 141602. <https://doi.org/10.1016/j.msea.2021.141602>.
- Prashanth, K. G., S. Scudino, H. J. Klauss, K. B. Surreddi, L. Löber, Z. Wang, A. K. Chaubey, U. Kühn, and J. Eckert. 2014. "Microstructure and Mechanical Properties of Al-12Si Produced by Selective Laser Melting: Effect of Heat Treatment." *Materials Science and Engineering: A* 590: 153–160. <https://doi.org/10.1016/j.msea.2013.10.023>.
- Røyset, J., and N. Ryum. 2005. "Some Comments on the Misfit and Coherency Loss of Al<sub>3</sub>Sc Particles in Al<sub>3</sub>Sc Alloys." *Scripta Materialia* 52: 1275–1279. <https://doi.org/10.1016/j.scriptamat.2005.02.023>.
- Sonawane, A., G. Roux, J. J. Despres, and G. Martin. 2021. "Cracking mechanism and its sensitivity to processing conditions during laser powder bed fusion of a structural aluminum alloy." *Materialia* 15: 100976. <http://doi.org/10.1016/j.mtla.2020.100976>.
- Sun, Z. J., Y. Ma, D. Ponge, S. Zaefferer, E. A. Jäggle, B. Gault, A. D. Rollett, and D. Raabe. 2022. "Thermodynamics-guided Alloy and Process Design for Additive Manufacturing." *Nature Communications* 13: 4361. <https://doi.org/10.1038/s41467-022-31969-y>.
- Sun, Z. J., X. P. Tan, C. C. Wang, M. Descoins, D. Mangelinck, S. B. Tor, E. A. Jäggle, S. Zaefferer, and D. Raabe. 2021. "Reducing hot Tearing by Grain Boundary Segregation Engineering in Additive Manufacturing: Example of an Al<sub>x</sub>CoCrFeNi High-Entropy Alloy." *Acta Materialia* 204: 116505. <https://doi.org/10.1016/j.actamat.2020.116505>.
- Sun, W., Y. Zhu, R. Marceau, L. Y. Wang, Q. Zhang, X. Gao, and C. Hutchinson. 2019. "Precipitation Strengthening of Aluminum Alloys by Room-Temperature Cyclic Plasticity." *Science* 363: 972–975. <https://doi.org/10.1126/science.aav7086>.
- Tan, Q. Y., J. Q. Zhang, Q. Sun, Z. Q. Fan, G. Li, Y. Yin, Y. G. Liu, and M. X. Zhang. 2020. "Inoculation Treatment of an Additively Manufactured 2024 Aluminium Alloy with Titanium Nanoparticles." *Acta Materialia* 196: 1–16. <https://doi.org/10.1016/j.actamat.2020.06.026>.
- Thijs, L., M. L. M. Sistiaga, R. Wauthle, Q. Xie, J. Kruth, and J. V. Humbeeck. 2013. "Strong Morphological and Crystallographic Texture and Resulting Yield Strength Anisotropy in Selective Laser Melted Tantalum." *Acta Materialia* 61: 4657–4668. <https://doi.org/10.1016/j.actamat.2013.04.036>.
- Voisin, T., J. Forien, A. Perron, S. Aubry, N. Bertin, A. Samanta, A. Baker, and Y. M. Wang. 2021. "New Insights on Cellular Structures Strengthening Mechanisms and Thermal Stability of an Austenitic Stainless Steel Fabricated by Laser Powder-bed-Fusion." *Acta Materialia* 203: 116476. <https://doi.org/10.1016/j.actamat.2020.11.018>.
- Wang, P., C. Gammer, F. Brenne, K. G. Prashanth, R. G. Mendes, M. H. Rummeli, T. Gemming, J. Eckert, and S. Scudino. 2018. "Microstructure and Mechanical Properties of a Heat-Treatable Al-3.5Cu-1.5Mg-1Si Alloy Produced by Selective Laser Melting." *Materials Science and Engineering: A* 711: 562–570. <https://doi.org/10.1016/j.msea.2017.11.063>.
- Wang, Y. T., R. D. Li, T. C. Yuan, L. Zou, M. B. Wang, and H. O. Yang. 2021. "Microstructure and Mechanical Properties of Al-Fe-Sc-Zr Alloy Additively Manufactured by Selective Laser Melting." *Materials Characterization* 180: 111397. <https://doi.org/10.1016/j.matchar.2021.111397>.
- Wang, Z. H., X. Lin, N. Kang, Y. L. Hu, J. Chen, and W. D. Huang. 2020. "Strength-ductility Synergy of Selective Laser Melted Al-Mg-Sc-Zr Alloy with a Heterogeneous Grain Structure." *Additive Manufacturing* 34: 101260. <https://doi.org/10.1016/j.addma.2020.101260>.
- Wang, J. Y. F. P., H. L. Yang, L. J. Yang, Y. Y. Zhang, Z. L. Liu Zhang, and S. X. Ji. 2022. "Effect of Heat Treatment on the Microstructure and Mechanical Properties of an Al-5Mg2Si-2Mg Alloy Processed by Laser Powder bed Fusion." *Journal of Alloys and Compounds* 920: 165944. <https://doi.org/10.1016/j.jallcom.2022.165944>.
- Wang, X. J., L. C. Zhang, M. H. Fang, and T. B. Sercombe. 2014. "The Effect of Atmosphere on the Structure and Properties of a Selective Laser Melted Al-12Si Alloy." *Materials Science and Engineering: A* 597: 370–375. <https://doi.org/10.1016/j.msea.2014.01.012>.
- Warmuzek, M., A. Polkowska, V. Boyko, E. Czekaj, K. Mikhalenkov, and K. Saja. 2021. "Microstructural Evolution of an Al-Mg-Si-Mn-Fe Alloy due to Ti and P Addition." *International Journal of Materials Research* 112: 695–705. <https://doi.org/10.1515/ijmr-2020-7948>.
- Wei, P., Z. Y. Wei, Z. Chen, J. Du, Y. Y. He, J. F. Li, and Y. T. Zhou. 2017. "The AlSi10Mg Samples Produced by Selective Laser Melting: Single Track, Densification, Microstructure and Mechanical Behavior." *Applied Surface Science* 408: 38–50. <https://doi.org/10.1016/j.apsusc.2017.02.215>.
- Wei, W., J. C. Xiao, C. F. Wang, Q. Cheng, F. J. Guo, Q. He, M. S. Wang, S. Z. Jiang, and C. X. Huang. 2022. "Hierarchical Microstructure and Enhanced Mechanical Properties of SLM-Fabricated GH5188 Co-Superalloy." *Materials Science and Engineering: A* 831: 142276. <https://doi.org/10.1016/j.msea.2021.142276>.
- Yang, H. L., S. X. Ji, and Z. Y. Fan. 2015. "Effect of Heat Treatment and Fe Content on the Microstructure and Mechanical Properties of die-Cast Al-Si-Cu Alloys." *Materials & Design* 85: 823–832. <https://doi.org/10.1016/j.matdes.2015.07.074>.

- Yang, H. L., Y. Y. Zhang, J. Y. Wang, Z. L. Liu, C. H. Liu, and S. X. Ji. 2021. "Additive Manufacturing of a High Strength Al-5Mg<sub>2</sub>Si-2Mg Alloy: Microstructure and Mechanical Properties." *Journal of Materials Science & Technology* 91: 215–223. <https://doi.org/10.1016/j.jmst.2021.02.048>.
- Zhang, L. F., J. W. Gao, L. N. W. Damoah, and D. G. Robertson. 2012. "Removal of Iron from Aluminum: A Review." *Mineral Processing and Extractive Metallurgy Review* 33: 99–157. <https://doi.org/10.1080/08827508.2010.542211>.
- Zhang, D. Y., D. Qiu, M. A. Gibson, Y. F. Zheng, H. L. Fraser, D. H. StJohn, and M. A. Easton. 2019. "Additive Manufacturing of Ultrafine-Grained High-Strength Titanium Alloys." *Nature* 576: 91–95. <https://doi.org/10.1038/s41586-019-1783-1>.
- Zhang, F., C. Zhang, S. M. Liang, D. C. Lv, and W. S. Cao. 2020. "Simulation of the Composition and Cooling Rate Effects on the Solidification Path of Casting Aluminum Alloys." *Journal of Phase Equilibria and Diffusion* 41: 793–803. <https://doi.org/10.1007/s11669-020-00834-0>.
- Zhang, C., Y. Zhou, K. Wei, Q. D. Yang, J. H. Zhou, H. Zhou, X. Y. Zhang, and X. J. Yang. 2023. "High Cycle Fatigue Behaviour of Invar 36 Alloy Fabricated by Laser Powder bed Fusion." *Virtual and Physical Prototyping* 18: 2190901. <https://doi.org/10.1080/17452759.2023.2190901>.
- Zhou, Y., S. F. Wen, C. Wang, L. C. Duan, Q. S. Wei, and Y. S. Shi. 2019. "Effect of TiC Content on the Al-15Si Alloy Processed by Selective Laser Melting: Microstructure and Mechanical Properties." *Optics & Laser Technology* 120: 105719. <https://doi.org/10.1016/j.optlastec.2019.105719>.
- Zhu, X. Z., X. X. Dong, P. Blake, and S. X. Ji. 2021. "Improvement in as-Cast Strength of High Pressure die-Cast Al-Si-Cu-Mg Alloys by Synergistic Effect of Q-Al<sub>5</sub>Cu<sub>2</sub>Mg<sub>8</sub>Si<sub>6</sub> and θ-Al<sub>2</sub>Cu Phases." *Materials Science and Engineering: A* 802: 140612. <https://doi.org/10.1016/j.msea.2020.140612>.
- Zhu, Z. G., F. L. Ng, H. L. Seet, W. J. Lu, C. H. Liebscher, Z. Y. Rao, D. Raabe, and S. M. L. Nai. 2022. "Superior Mechanical Properties of a Selective-Laser-Melted AlZnMgCuScZr Alloy Enabled by a Tunable Hierarchical Microstructure and Dual-Nanoprecipitation." *Materials Today* 52: 90–101. <https://doi.org/10.1016/j.mattod.2021.11.019>.
- Zhu, X., H. Yang, X. Dong, and S. Ji. 2019. "The Effects of Varying Mg and Si Levels on the Microstructural Inhomogeneity and Eutectic Mg<sub>2</sub>Si Morphology in die-Cast Al-Mg-Si Alloys." *Journal of Materials Science* 54: 5773–5787. <https://doi.org/10.1007/s10853-018-03198-6>.